WILEY-VCH

Microstructural Welding Engineering of Carbon Nanotube/Polydimethylsiloxane Nanocomposites with Improved Interfacial Thermal Transport

Fei Zhang [#], Yuxuan Sun[#], Lei Guo, Yinhang Zhang, Dan Liu, Wei Feng[*], Xi Shen[*], Qingbin Zheng[*]

F. Zhang, Y. Sun, L. Guo, Y. Zhang, D. Liu, Q. B. Zheng
School of Science and Engineering, The Chinese University of Hong Kong, Shenzhen, Shenzhen, Guangdong 518172, P. R. China
E-mail: zhengqingbin@cuhk.edu.cn

F. Zhang
Institute of Flexible Electronics Technology of THU, Zhejiang, Jiaxing, 314006 China
Department of Engineering Mechanics, Tsinghua University, Beijing, 100084, China

W. Feng
School of Materials Science and Engineering, Tianjin University, Tianjin, 300072, P.R. China
E-mail: weifeng@tju.edu.cn

X. Shen
Department of Aeronautical and Aviation Engineering, The Hong Kong Polytechnic University, Hung Hom, Kowloon, Hong Kong SAR, China
E-mail: xi.shen@polyu.edu.hk

X. Shen
The Research Institute for Sports Science and Technology, The Hong Kong Polytechnic University, Hung Hom, Kowloon, Hong Kong SAR, China

#These authors contributed to the work equally.

Keywords: Carbon nanotube network, Interfacial welding, Interfacial thermal resistance, Thermal conductivity

Abstract: Carbon nanotube (CNT) reinforced polymer nanocomposites with high thermal conductivity show a promising prospect in thermal management of next-generation electronic devices due to their excellent mechanical adaptability, outstanding processability and superior flexibility. However, interfacial thermal resistance between individual CNT significantly hinders the further improvement in thermal conductivity of CNT-reinforced nanocomposites. Herein, we report an interfacial welding strategy to construct graphitic structure welded CNT (GS-w-CNT) networks. Notably, the obtained GS-w-CNT/polydimethylsiloxane (PDMS) nanocomposite with a GS loading of 4.75 wt% preserves a high thermal conductivity of 5.58 W m^{-1} K^{-1} with a 410% enhancement as compared to a pure CNT/PDMS nanocomposite. Molecular dynamics simulations are utilized to elucidate the effect of interfacial welding on the heat transfer behaviour, revealing that the GS welding degree plays an important role in reducing both phonon scattering in the GS-w-CNT structure and interfacial thermal resistance at the interfaces between CNT. The unique welding strategy provides a new route to optimize the thermal transport performance in filler reinforced polymer nanocomposites, promoting their applications in next-generation microelectronic devices.

1. Introduction

Polymer-based materials have attracted extensive interest for thermal management in high-power microelectronic devices owing to their outstanding properties including superior flexibility, lightweight, excellent processability and low cost [1, 2]. Unfortunately, most polymers possess a relatively low thermal conductivity ranging from 0.1 to 0.5 W m^{-1} K^{-1} [3, 4]. Although designing a brand new polymer may exhibit intrinsically high thermal conductivity, a simple and effective approach to enhance the thermal conductivity of polymers is incorporating highly thermally conductive fillers such as metal [5-7], ceramic [8, 9], and carbon-based materials [10-18], into polymers. Combining lightweight with excellent thermal conductivity, carbon-based materials including graphite [17, 18], graphite oxide [11, 19], graphene [13, 14] and carbon nanotube (CNT) [12, 15] are considered as potential fillers. Especially, CNT appears to be a promising thermally conductive filler due to its outstanding thermal conductivity (~1000-3000 W m^{-1} K^{-1}) [20-23]. According to Maxwell's equation, 1 vol% loading of CNT is supposed to lead to a 10-fold increase in the thermal conductivity of polymer nanocomposites [24]. However, the high interfacial thermal resistance in CNT-reinforced nanocomposites significantly restricts the utilization of CNT's superior thermal conductivity, resulting in lower thermal conductivity than that expected from theoretical calculations [25, 26].

In general, interfacial thermal resistance in CNT-reinforced nanocomposites can be divided into the thermal resistance at the interface between matrix and CNT, and the thermal resistance between CNT fillers [1, 27]. The interfacial thermal resistance between polymer matrix and CNT filler is attributed to the tremendous mismatch of their phonon spectra, which is difficult to eliminate [28]. For instance, the thermal conductivity of a 3D random array of CNTs is calculated to be lower than that of conventional amorphous polymers [29]. A single-walled carbon nanotube (SWCNT) aerogel only showed a thermal conductance as low as 12 pW K^{-1}at the tube–tube junctions [30]. The limited physical contact of the neighbouring CNTs significantly hinders the heat transfer [31, 32].

By using molecular dynamic (MD) simulation, it is predicted that a pillared-graphene and CNT network connected by covalent bonds offers a significant enhancement of thermal conductivity due to the decrease of interfacial thermal resistance [33-35]. Similarly, the interfacial thermal resistance among CNT fillers can be substantially decreased *via* interfacial welding to bridge the gaps between adjacent tubes [3], which can offer efficient phonon transmission to avoid severe phonon scattering at the interface and thus significantly improve thermal transport properties [36]. Interfacial welding is also an effective strategy to improve thermal conductivity of polymer nanocomposites [37, 38]. For example, 3D graphene skeleton welded by carbonized polyimide (PI) provided two folds increase in thermal conductivity [36]. The covalently-bonded CNT junctions provided a 2-fold drop in the interfacial thermal resistance compared to randomly stacked CNT [37]. In our previous work [39], graphite layers welded 3D CNT networks showed much improved thermal conductivity due to the effective phonon and stress transfer at the junctions. A significant enhancement of the thermal conductivity was also observed for boron nitride [40] and silicon carbide nanowire network [41] by interfacial welding. However, an in-depth investigation on the phonon transmission mechanism of the welding interface is still lacking.

Herein, a combined experiment and molecular dynamics simulation study was conducted to systematically investigate the influence of interfacial welding on the thermal conductivity of CNT-reinforced polymer nanocomposites. GS-w-CNT networks with different welding degree were constructed *via* impregnation process followed by thermal annealing strategy. The produced GS-w-CNT/polydimethylsiloxane nanocomposites exhibited a superior thermal conductivity to that of CNT/ PDMS nanocomposites without interfacial welding. To elucidate the role of interfacial welding in improving the thermal conductivity of GS-w-CNT/PDMS nanocomposites, MD simulations were performed to investigate the thermal transport behaviours of GS-w-CNT/PDMS nanocomposites. To get an insight into the welding

enhancement mechanism, the phonon vibration power spectra were analyzed to reveal the effect of interfacial welding on the heat transfer within the CNT networks.

2. Results and Discussion

2.1. Preparation of GS-w-CNT/PDMS

Figure 1a schematically depicts the synthesis route of the GS-w-CNT/PDMS nanocomposites. The initial CNT network was synthesized by in-situ chemical vapor deposition (CVD) method based on our previous work [39, 42]. Specifically, individual CNT intertwined with each other and formed self-supported CNT networks during the CVD process. After directly immersing in a poly (amic acid) (PAA) solution, the CNT network was coated by PAA uniformly. Due to the capillary force generated between PAA solution and CNTs, PAA was preferentially deposited across the junctions between individual CNT during the coating process [43, 44]. PAA was then converted to PI after the thermal imidization process. The converted PI served as "glue" to physically join adjacent CNTs and realize the interconnection of CNT network. Thereafter, the network was transferred to GS-w-CNT *via* the graphitization treatment. Besides, the weight ratio of GS was controlled by changing PAA concentration and repeated cycles of the impregnation process so that a series of GS-w-CNT networks with the density from 18.2 mg cm^{-3} to 71.6 mg cm^{-3} were prepared. Since the welded GS structure bridged and strengthened the discontinuous CNTs, the obtained GS-w-CNT networks exhibited a robust mechanical performance. As shown in the **Figure S1**, the initial CNT network presented almost 60% permanent deformation due to the weak connection of individual CNTs, which obstructed the transfer of stress between adjacent CNTs. In contrast, there was no permanent compressive deformation as a result of efficient stress transfer at the GS welded CNT junctions. Additionally, with the increasing welding degree (density from 31.5 mg cm^{-3} to 71.6 mg cm^{-3}), the compressive strain of GS-w-CNT structure showed a steady decrease from about 10% to 3%. Apparently, the GS structure that welded in the CNT network enhanced the structural integrity and stability. Finally, the resultant structures were immersed into PDMS precursor solution and cured at 70 ºC to fabricate GS-w-CNT/PDMS nanocomposites with GS-w-CNT weight ratio of 1.77 wt%, 2.97 wt%, 4.31 wt% and 6.52 wt%.

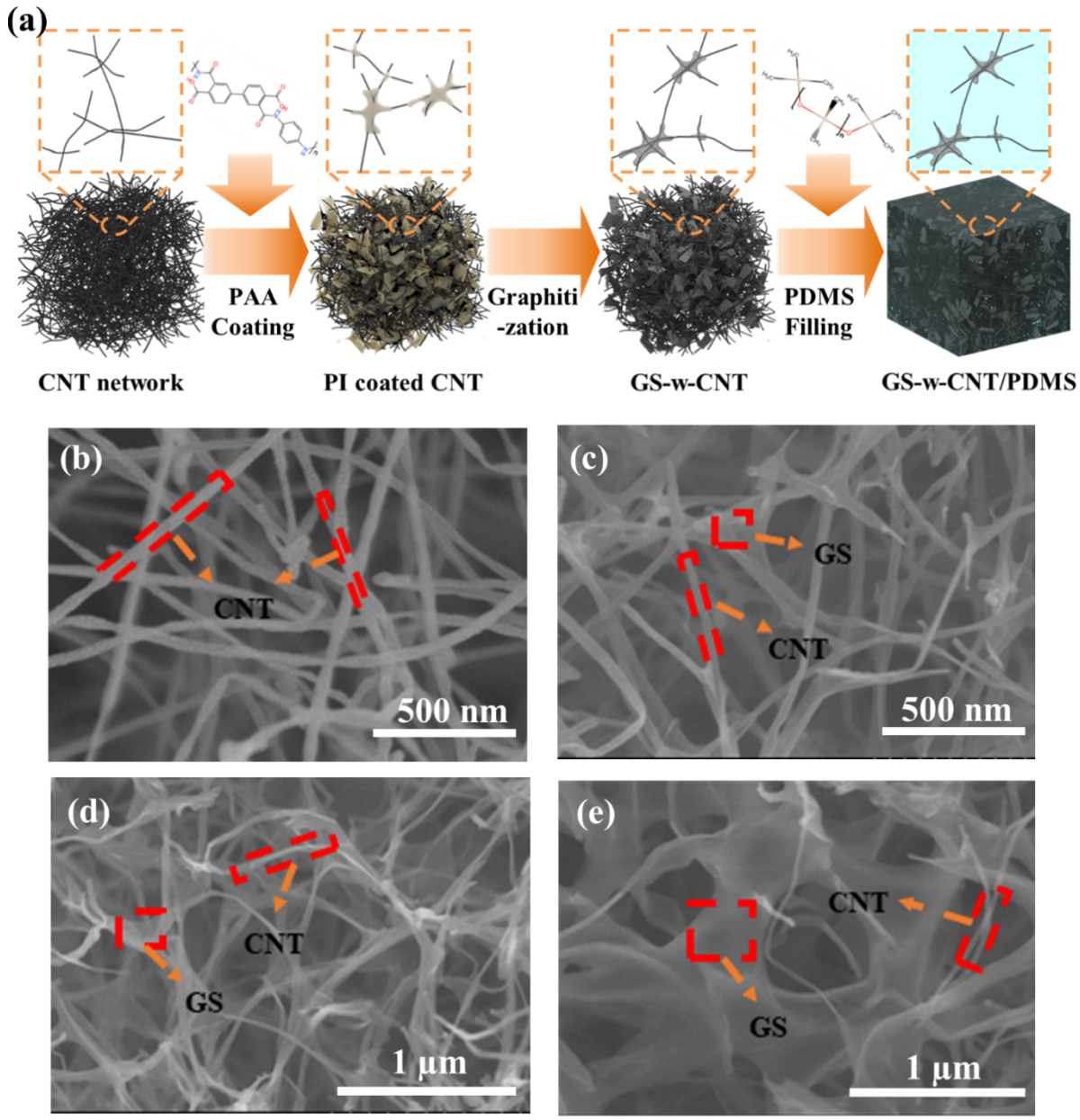

Figure 1. (a) Schematic illustration for the fabrication process of GS-w-CNT/PDMS. (b-e) Morphology of CNT network with 0 wt%, 1.2 wt%, 2.54 wt%, and 4.75 wt% GS loading.

Figures 1b-e show the morphology evolution of pristine CNT network and CNT network welded with increasing GS loading. The initial CNT network (**Figure 1b**) was composed of randomly intertwined CNTs with open cell porous structure. When 1.20 wt% GS was introduced (**Figure 1c**), the area of CNT network connected by GS is limited. Hence, neighbouring CNTs with bigger gap were unable to be connected. With the GS contents increasing to 2.54 wt% and 4.75 wt% (**Figure 1d-e**), GS were gradually wrapping the CNT junctions, forming an interconnected porous structure. The CNT junction structures with different GS loading (0, 1.20 wt%, 2.54 wt% and 4.75 wt%) were confirmed *via* high-

magnification transmission electron microscope (TEM) (**Figure 2a-d**). The welded CNT junction area continueously increased with increasing GS loadings from 0 to 4.75 wt %. It is observed that individual CNTs were bridged by the GS as shown in the high-magnification TEM image (**Figure 2e**). Besides, from the fast Fourier transform (FFT) diffraction pattern (**Figure 2f**), it can be seen that the welded GS possessed a regular lattice structure.

The crystal structure evolution of CNT networks after welding GS was characterized by Raman spectra (**Figure 2g**) and X-ray diffraction (XRD) (**Figure 2h**). In Raman spectra, comparing to the initial CNT network, the intensity ratio of D-band (1350 cm^{-1}) to G band (1580 cm^{-1}) of GS-w-CNT was decreased from 0.736 to 0.097, revealing that the disordered sp^3 bonding was restored to the graphitic sp^2 bonding under high-temperature graphitization. In addition, the decrease in half-width of G band suggests the formation of a well-ordered graphite structure. In XRD pattern, the typical diffraction peak of (0 0 2) crystal plane to CNT and GS was around 26°. After GS welding, the intensity enhancement of the (0 0 2) crystal plane, as well as the lower peak at 45°((1 0 0) crystal plane), confirms the high graphitization degree of GS-w-CNT structure [45]. The relatively high crystallinity portion of the welding structures guarantees a better structural integrity and efficient thermal transfer in contrast to amorphous carbon or other disordered graphitic structure [39, 46].

To investigate the improvement in the thermal conductivity of GS-w-CNT structures, the GS-w-CNT structures with different density were immersed into PDMS to fabricate the GS-w-CNT/PDMS nanocomposites. The morphologies of the GS-w-CNT/PDMS are shown in **Figures 2i** and **j**. Welded CNT frameworks were evenly dispersed and embedded in the PDMS matrix. The detailed GS-w-CNT structures in PDMS is shown in high-resolution TEM images (**Figure 2k**). Owing to the strong interaction exhibited between the π-conjugated structure in GS-w-CNT and PDMS chains [47, 48], PDMS was uniformly coated on the networks and limited damage was generated during PDMS infiltration.

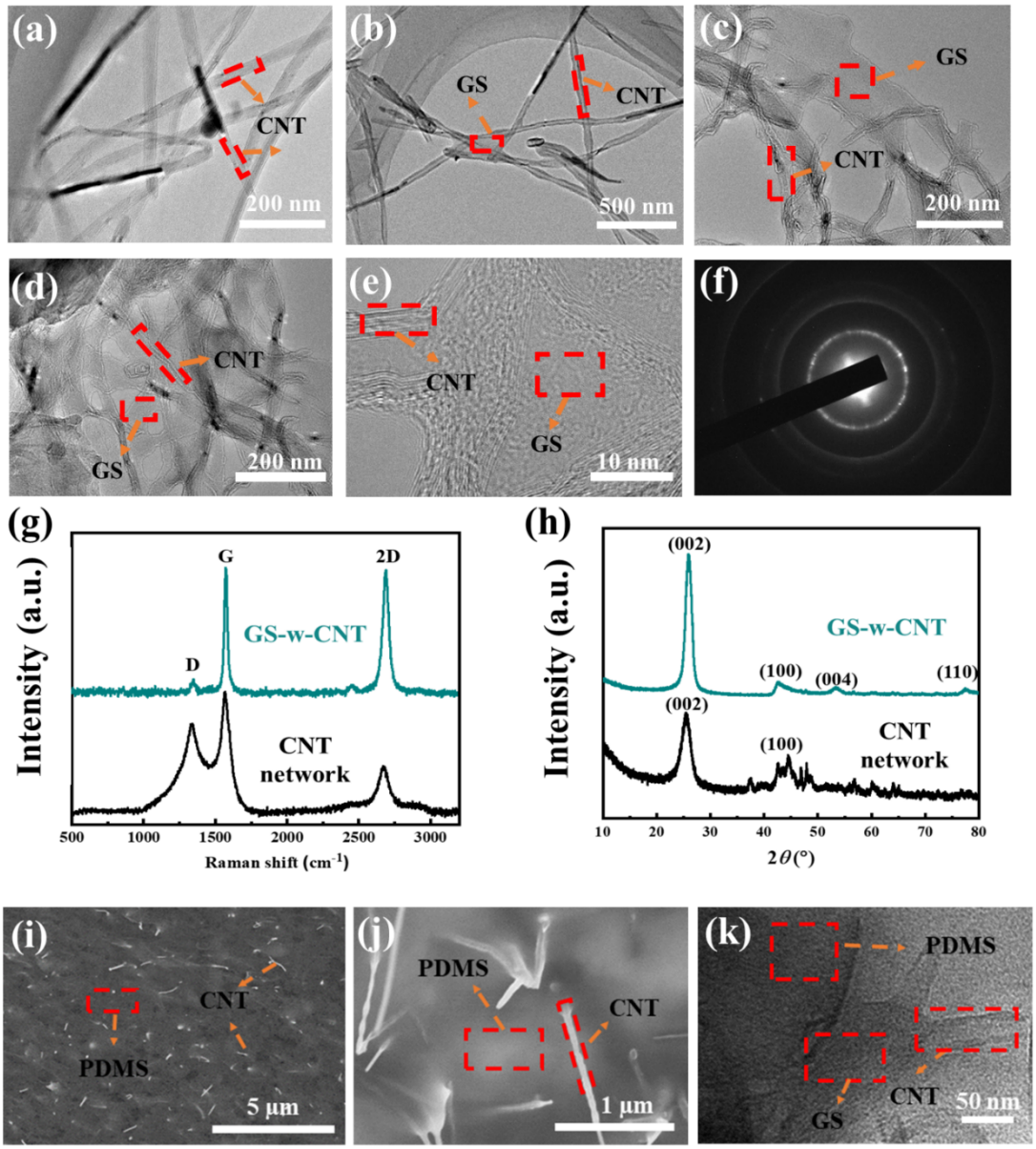

Figure 2. (a-d) TEM images of pristine CNT network (a) and CNT network welded with 1.2 wt% (b), 2.54 wt% (c), and 4.75 wt% (d) GS. (e) High-resolution image of GS-w-CNT. (f) FFT diffraction pattern of GS-w-CNT. Raman spectra (g) and XRD patterns (h) of CNT networks and CNT network with 4.75 wt% welded GS loading. (i-j) Morphology of GS-w-CNT distribution in PDMS with low (i) and high (j) magnifications. (k) High-resolution morphology of welded CNT junction in PDMS.

2.2. Thermal conductivity of GS-w-CNT/PDMS

Figure 3a summarizes the thermal conductivity of the GS-w-CNT/PDMS nanocomposites. It is shown that GS-w-CNT/PDMS possessed a higher thermal conductivity than CNT/PDMS nanocomposite. Besides, the thermal conductivity of GS-w-CNT/PDMS nanocomposite continuously increased with the ascending loading of welding GS and reached 5.58 W m^{-1} K^{-1}

at 6.52 wt% GS-w-CNT loading, which is 410% higher than that of CNT/PDMS. Compared with the reported thermally conductive nanocomposites filled with 3D carbon-based network, the GS-w-CNT/PDMS nanocomposite prepared in this work showed higher thermal conductivity with similar filler content, as shown in **Figure 3b** and **Table S1**.

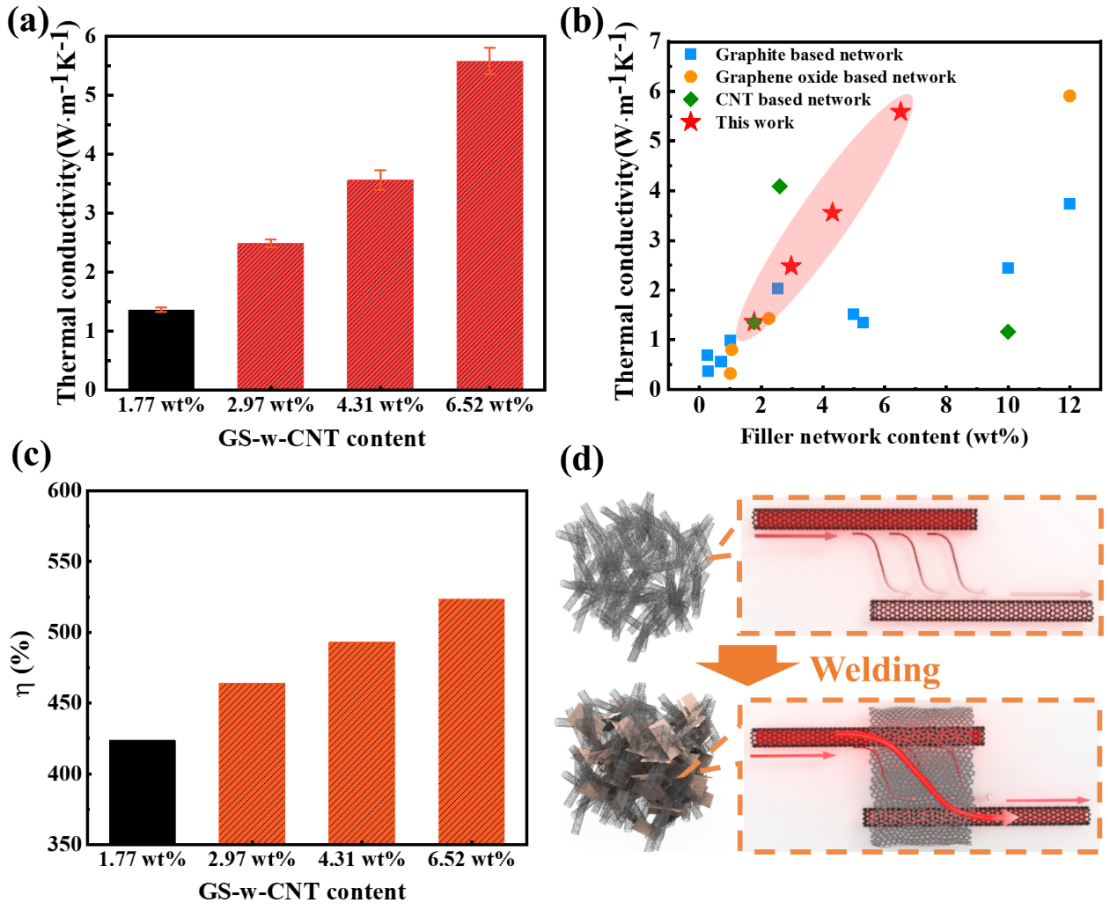

Figure 3. (a) Thermal conductivity of GS-w-CNT/PDMS nanocomposite with various GS-w-CNT contents (black colour represents the original CNT/PDMS). (b) Comparison of the thermal conductivity of polymer composites with 3D network fillers. (c) Thermal conductivity efficiency of GS-w-CNT/PDMS nanocomposite with various GS-w-CNT contents (black colour represents the original CNT/PDMS). (d) Schematic of the thermal transport enhancement mechanism after GS welding in CNT networks.

Thermal conductivity efficiency η, which can be used to describe the enhancement that GS-w-CNT structure provided to the thermal conductivity of PDMS matrix, is defined as follows [20]:

$$\eta = \frac{k_c - k_m}{M_f k_m} 100\% \quad (1)$$

where k_c and k_m are thermal conductivities of the nanocomposite and matrix (0.16 W m^{-1} K^{-1} for pure PDMS) respectively, and M_f represents the filler weight fraction of nanocomposites. As shown in **Figure 3c**, an excellent value of η (523%) was observed for GS-w-CNT/PDMS nanocomposite with 6.52 wt% GS-w-CNT in contrast to 423% for original CNT/PDMS nanocomposite. More importantly, a positive correlation between the weight ratio of welded GS and η was observed. When GS-w-CNT content was 2.97 and 4.31 wt%, the nanocomposite exhibited a thermal conductivity of 2.54 W m^{-1} K^{-1} with 463% enhancement and 3.56 W m^{-1} K^{-1} with 493% enhancement respectively. As schematically shown in **Figure 3d,** the thermal energy cannot transfer efficiently in CNT junctions due to the interfacial thermal resistance between adjacent CNT. Once the GS structures were welded on the CNT junction, the strong conjugated interactions provided an efficient thermal transport by phonons across the interface. Additionally, the contact area between CNT and GS continuously increased as the increasing of GS content. Consequently, the integrity of the interconnected GS-w-CNT networks were enhanced and the thermal conductivity of the nanocomposite was improved.

2.3. Molecular dynamics simulation

As shown in **Figure 4a**, two SWCNTs are aligned along *z*-direction, which are sandwiched between two parrallel graphene sheets to simulate the GS welding structure. The length of graphene sheet is gradually increased from 2.6 nm to 7.9 nm to simulate different GS loading in the experiment **(Figure 4b)**. PDMS chains are then packed into the simulation box to obtain the GS-w-CNT/PDMS model (**Figure 4c)**. The utilization of a single-chain PDMS to represent amorphous PDMS is popularly used in MD simulations [49-52]. Although the thermal conductivity exhibits a slight increase with the increasing length of the PDMS chain [50], the effect of PDMS chain length is negligible when forming a amorphous PDMS system [52]. Besides, periodic boundary conditions are set along *x*, *y*, and *z* directions. After constructing GS-w-CNT/PDMS models with weight ratio from 14.55 wt% to 26.16 wt% (**Figure S2 a-d**), the structures are further optimized to reach thermal equilibrium for thermal conductivity calculation. During the process, GS can be wrapped around the CNTs driven by van der Waals interactions between GS and CNT (**Figure S2e and f).**

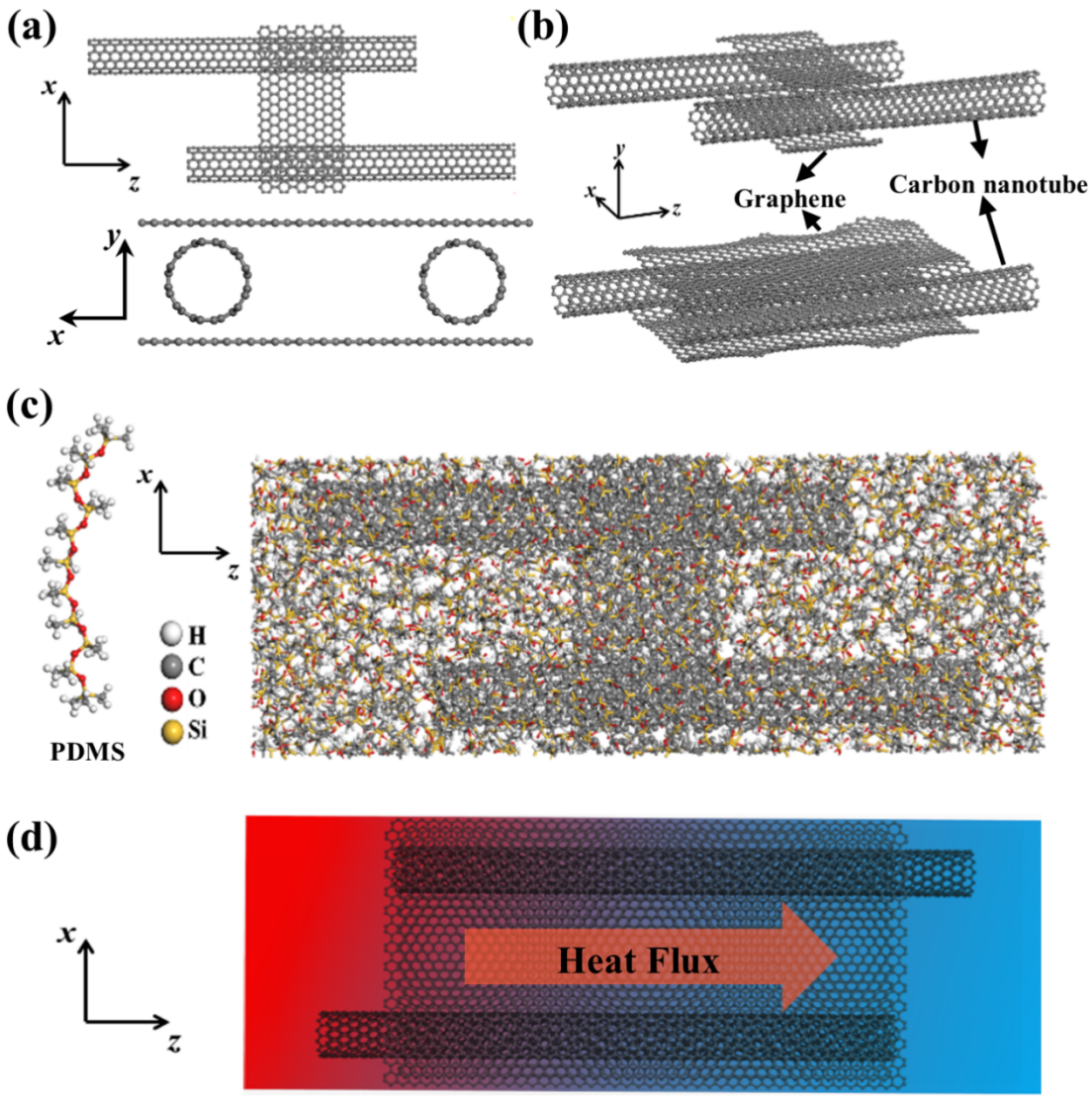

Figure 4. (a–c) Molecular models of (a) GS-w-CNT, (b) GS-w-CNT with increasing weight ratio of GS, and (c) GS-w-CNT/PDMS. (d) GS-w-CNT model used in RNEMD method.

Reverse non-equilibrium molecular dynamics (RNEMD) method is applied to investigate the thermal transport in the GS-w-CNT/PDMS (**Figure 4d**). Once thermal equilibrium is reached, a constant temperature gradient and heat flux is obtained. Due to the partially diffusive transport behaviours in the hot and cold slabs, temperature gradient curve at the beginning and the end (**Figure 5a**) shows a nonlinear temperature distribution. To avoid fluctuation effects, the temperature gradient of the model is extracted from linear fitting of the middle part of the curve (2 nm to 6.5 nm). The calculated thermal conductivity of pure PDMS and pristine CNT/PDMS (14.55 wt% CNT) is 0.13 W m^{-1} K^{-1} and 0.82 W m^{-1} K^{-1} respectively. After introducing GS, the obtained GS-w-CNT/PDMS with GS-w-CNT loading of 19.79 wt% shows a higher thermal conductivity of 0.95 W m^{-1} K^{-1}. Notably, the thermal conductivity of GS-w-

CNT/PDMS increases with increasing GS and exhibits a thermal conductivity value of 1.45 W m^{-1} K^{-1} (28.54 wt% GS-w-CNT) with an improvement of 176% against CNT/PDMS. When the length of CNT and graphene is much lower than the mean free path of the energy-carrying phonons, the thermal conductivity of CNT and graphene is proportional to their length [53-55]. For CNT and GS in the experiment, the mean free path is more than 100 nm [56, 57]. However, due to the computational limitations, the length of CNT and graphene model in the simulation was set as 7.8 nm and 7.9 nm respectively, which is much smaller than that in experiment (>100 nm). Therefore, the thermal conductivity of GS-w-CNT simulation model is much lower than the value obtained in the experiments. Nevertheless, the simulation is still tremendously important to understand the thermal transport behavior at the interfaces of GS and CNT.

The enhanced thermal transport performance can be attributed to the thermal resistance reduction after GS welding. Since the thermal resistance (R) across CNT junctions is the main source of thermal resistance in CNT network, RNEMD method is applied to investigate R between GS and CNTs **(Figure S3)**. By setting the heat flux along y-direction (**Figure 5c),** which is perpendicular to the GS and CNT, R is determined as follows [58].

$$R = \frac{\Delta T}{J} \tag{2}$$

where ΔT represents the temperature jump at the CNT and GS interface, and J is the heat flux. **Figure 5d** shows the R values of GS-w-CNT structures as a function GS welding content. The interfacial thermal resistance decreases from 1.68×10^{-8} m^2 K W^{-1} to 6.98×10^{-9} m^2 K W^{-1} with the increasing GS welding content from 19.79 wt% to 28.54 wt%. From a microscopic point of view, thermal conduction across GS-CNT interface is accomplished through the interaction between the two groups of C atoms at the interface of GS and CNT. To elucidate the correlation between interface binding energy and the interface thermal resistance in GS-w-CNT structure, the relative interface binding energy (E_I) is calculated by the following equation [59, 60].

$$E_I = \left| E_T - (E_g + E_{CNTs}) \right| \tag{3}$$

where E_T, E_g and E_{CNTs} is the energy for the total structure, GS and CNTs respectively (**Figure 5c**). It is found that the interfacial binding energy increases with increasing GS welding (**Figure 5d**) due to the strong π-π interactions between CNT and GS with hexagonal carbon rings. The enhanced interface binding strength will certainly reduce the interfacial thermal resistance between adjacent CNT due to the reduced phonon scattering in nanoscale, which strongly improves thermal energy transport across CNT interfaces.

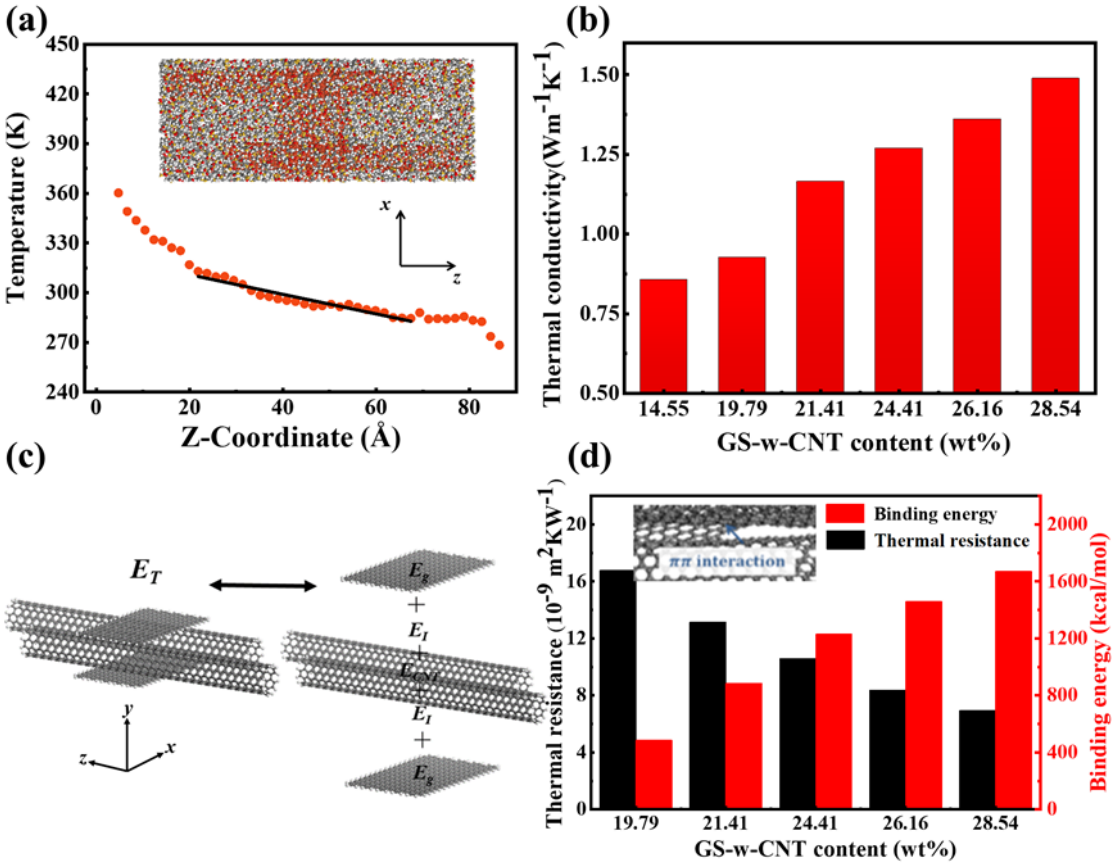

Figure 5. (a) The temperature gradient in GS-w-CNT/PDMS along z-direction. (b) Thermal conductivities of GS-w-CNT/PDMS. (c) Models for thermal resistance and interfacial binding energy calculation. (d) Interfacial binding energy and thermal resistance between CNT and GS.

To further investigate the effects of GS welding on the phonon transport of GS-w-CNT/PDMS nanocomposites, the vibrational power spectrum (VPS) of PDMS and CNT and GS with various welding weight ratio are calculated. Larger overlap area of two VPS curves represents a stronger phonon coupling. It can be seen that the VPS curves of CNT and PDMS show a poor overlap in all frequencies **(Figure 6a)**. Compared with PDMS, the VPS curve of GS has a better match with that of CNT. It is seen from **Figure 6b** that the overlap range of the VPS of GS and CNTs is mainly distributed in 0-500 cm^{-1}. As the increasing of GS welding contents, the distribution ranges of VPS are gradually extended to 0-500 cm^{-1} and 1500-2000 cm^{-1}, respectively, leading to an increase of overlap between VPS curves of GS and CNT An overlapping factor (δ) is introduced to give a quantitative description to the match of VPS curve as follows: [61, 62]

$$\delta = \int H(\omega)\, d\omega \tag{4}$$

where $H(\omega)$ represents the normalized magnitude difference between two VPS curves at frequency ω. As shown in **Figure 6c,** δ only exhibits a value of 0.017 for the VPS curves of PDMS and CNT. Once the GS is introduced, δ gradually increases to 0.63 with a GS-w-CNT content of 28.54 wt%. It implies that phonon coupling in CNT network is significantly improved due to the GS welding, which provide more channels for thermal transport across the GS/CNT interface (**Figure 6d**). The result agrees with the relationships of interfacial thermal resistance and provide a good explanation for the decrease of interfacial thermal resistance with increasing GS welding content.

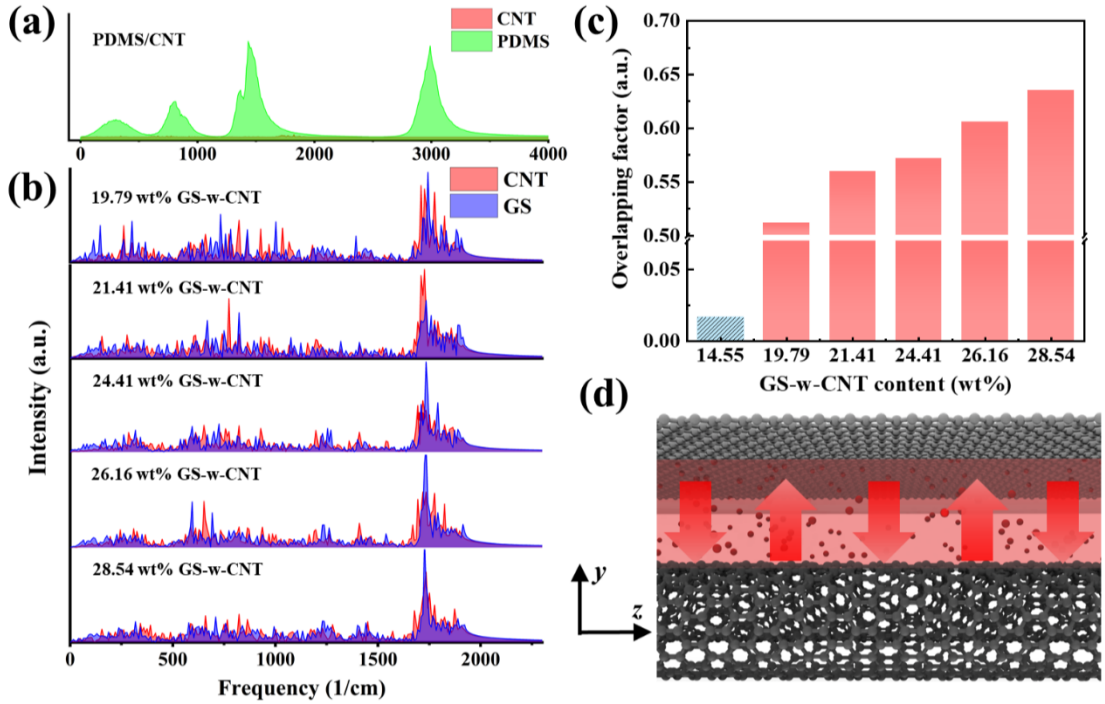

Figure 6. VPS of (a) CNT and PDMS and (b) CNT and GS-w-CNT with different weight percentage of GS welding. (c) Overlapping factors between the VPS curves of CNT, PDMS and different weight percentage of GS. (d) Schematic diagram of heat transferred by phonon coupling between CNT and GS (the arrows represent the transport direction).

Besides, the introduced GS also breaks the origin symmetries of CNTs such as reflection, translation, and rotation. Therefore, the vibrations of C atoms in CNT are affected by the interactions between GS and CNT. As a result, the coupling of the phonons in CNT along different directions is altered. To demonstrate this phenomenon, the total VPS curves of CNT are decomposed into *y*-direction and *z*-direction contribution (the direction is in line with that shown in **Figure 4c**) and plotted in **Figure 7a**. It is shown that as the GS-w-CNT weight ratio

rises from 14.55 wt% to 28.54 wt%, the peaks of *z*-direction VPS at 500-1000 cm^{-1} and 1500-2000 cm^{-1} gradually weakens, generating more overlap with the VPS of *y*-direction. The overlapping factor δ (**Figure 7b**) is increased by 15.62%, confirming the enhanced coupling between *y*-direction and *z*-direction phonons. After welding by GS, the vibrations of carbon atoms in CNT are affected by the π-π interactions between CNT and GS, especially the atoms that share same *z*-coordinate with that in GS. Consequently, as shown in **Figure 7c**, these carbon atoms in CNTs serve as scattering centres for the *y*-direction phonon transport, which enhances the coupling between *y*-direction phonons and *z*-direction phonons. Therefore, the energy associated with the z-direction phonons of CNT can be transmitted to that of *y*-directions phonons, promoting the efficiency of thermal conduction in the GS-w-CNT structure.

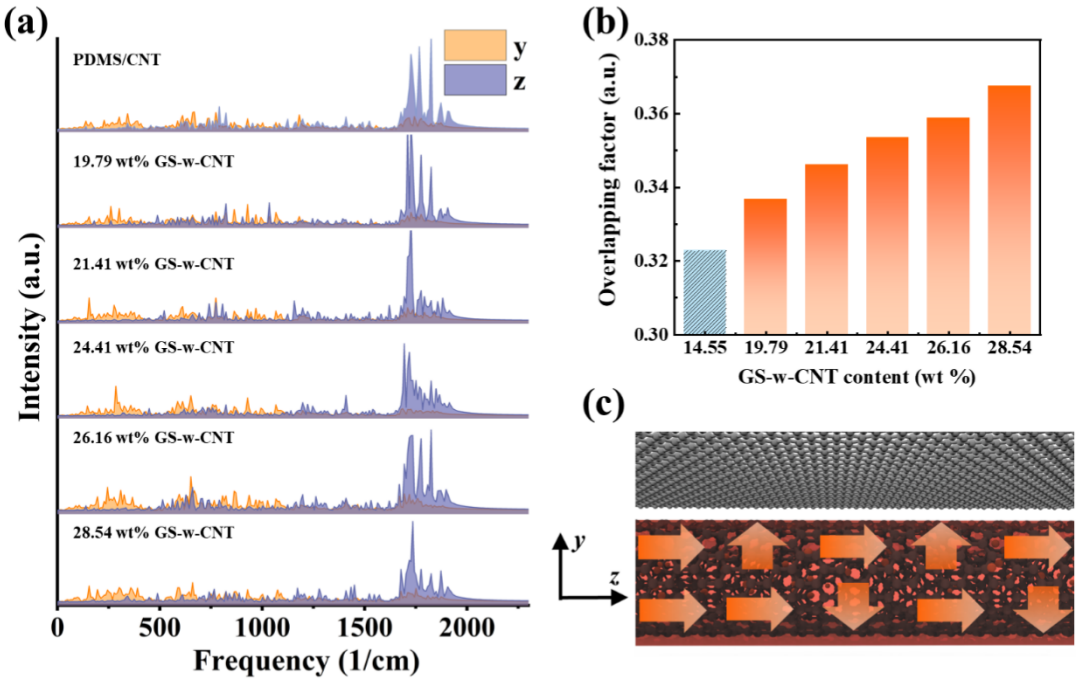

Figure 7. (a) VPS curves of CNT decomposed into *y* and *z*-directions. (b) Overlapping factors between CNT VPS curves in *y* and *z*-directions. (c) Schematic diagram of heat transfer by *y*-direction and *z*-direction phonon in CNT.

3. Conclusion

In summary, a combined experimental and MD simulations study is conducted to investigate the 3D CNT network reinforced PDMS nanocomposites with enhanced thermal conductivity *via* interfacial welding strategy. The experiment results show that the GS welding transforms the discontinuous CNT network into a 3D interconnected GS-w-CNT framework, leading to a significant increase in thermal conductivity. As the GS content increasing, the thermal

conductivity efficiency increases from 423% to 523%. Notably, the GS-w-CNT/PDMS nanocomposite presents a thermal conductivity of 5.58 W m^{-1} K^{-1} at a low GS-w-CNT loading of 6.52 wt%, which is 4.1 times higher than that of pristine CNT/PDMS. The MD simulation results confirmed the significant augmentation of heat transfer in the CNT junctions after welding with GS. With the increasing GS content, a higher interfacial binding energy and lower interfacial thermal resistance were observed between the adjacent CNT. Besides, phonon-phonon coupling at GS-CNT interface and phonon-phonon coupling along *y*-direction and *z*-direction in CNT are enhanced, which promote the heat exchange in GS-w-CNT structure. This study opens new possibilities in designing inter-connected filler network structure reinforced polymer nanocomposites with prominent thermal conductivity for thermal management in highly integrated electronics.

4. Experimental Section/Methods

Materials: PDMS (SYLGARD DC184) was provided by Dow Corning, Co., Ltd (USA). Pyromellitic dianhydride (PMDA, purity 96%) and 4, 4-oxydianiline (4, 4-ODA, purity 98%) used in the synthesis of PAA together with o-dichlorobenzene (purity 99%), ferrocene (purity 98%), dimethylacetamide (DMAC, purity 99.5%) and ethyl acetate (purity 99%) were all obtained from MACKLIN, Co., Ltd. (Shanghai, China).

Preparation of GS-w-CNT/PDMS nanocomposites: In-situ CVD was utilized for 3D CNT network growth. Specifically, 20 mm × 50 mm × 1 mm quartz sheets were fixed in quartz tube as the substrate for freestanding CNT network growing. The tube was then heated to 860 °C (15 °C min^{-1}) under an atmosphere of a gas mixture of Ar (800 sccm) and H_2 (160 sccm) for one hour. During the process, a microinjection pump continually injected a carbon source solution into the tube at a rate of 10 mL h^{-1}. The solution (0.06 g mL^{-1}) was a mixture of o-dichlorobenzene and ferrocene. After tube cooling down to room temperature naturally, the 3D CNT network was prepared with a density of 18.2 mg cm^{-3}. Subsequently, GS was welded in the as-achieved CNT network. In detail, PAA was selected as polymer precursor and synthesized by dissolving the same molar ratio of PDMA and ODA into DMAC solvent. After diluting the PAA to a solution with 2 wt% concentration by DMAC, the CNT network was immersed into solution under vacuum for 1 h to obtain PAA-coated CNT network. Then, thermal imidization of PAA-CNT network was performed under Ar atmosphere at 80, 150, 200, 250, 350 °C for 1h of each temperature stage. During the thermal imidization process, PAA was gradually converted into PI to form a PI-coated CNT network (PI-CNT). Finally, the GS-

w-CNT framework was fabricated by carbonizing and graphitizing the PI-CNT network at 1000 °C and 3000 °C, sequentially. The as-prepared networks possessed an ascending density of 31.5, 46.9 and 71.6 mg cm^{-3} respectively. The content of GS was tailored by changing PAA concentration and repeated cycles of the impregnation process. The concentration of PAA solution is adjusted from 3 wt% to 5 wt%. The CNT networks were immersed into PAA solution for once and twice respectively to obtain the samples with different amount of attached PAA. After undergoing a combination of thermal imidization and high-temperature graphitization process, GS-w-CNT networks with different GS content were obtained. The detailed preparation parameters of GS-w-CNT networks (CNT network, 1.77 wt % GS-w-CNT, 2.97 wt % GS-w-CNT, 4.31 wt% GS-w-CNT and 6.52 wt % GS-w-CNT.) are presented in **Table S2**. To produce GS-w-CNT/PDMS nanocomposite, PDMS curing and main agent were first mixed in a mass ratio of 1:10 in ethyl acetate. Then, GS-w-CNT were infiltrated with PDMS precursor solution at room temperature. After infiltration for 30 minutes, the samples were moved to a vacuum oven at ambient temperature for 2 hours to remove the air. Ultimately, the GS-w-CNT/PDMS nanocomposites were cured at 70 °C for 3 hours. For comparison, all the samples were prepared using the same procedure and cut into square slices (10 mm × 10 mm × 1 mm) for measurements.

Characterizations: Scanning electron microscope (SEM, MAIA 3, TESCAN, Czech) and TEM (JEM-F200, JEOL, Japan) were used to observe the morphology of CNT, GS-w-CNT and their nanocomposites. XRD (SmartLab, Rigaku, Japan) and Raman spectrometer (Renishaw, inVia, UK) was performed to study the crystal structure evolution in GS-w-CNT networks. The thermal conductivity of the GS-w-CNT/PDMS was calculated according to the equation [63]:

$$k = \alpha \times \rho \times C_p \quad (5)$$

where thermal diffusivity (α) of GS-w-CNT/PDMS was measured by the laser flash method. ρ and C_p are the sample density and specific heat capacity, respectively. A Laser flash analyzer (LFA 457, Netzsch, Germany) was used to measure the thermal diffusivity of GS-w-CNT/PDMS nanocomposites.

Molecular models: MD simulation was conducted to study the thermal transport between adjacent CNTs in GS-w-CNT/PDMS nanocomposites. GS-w-CNT/PDMS nanocomposite models were constructed using the Materials Studio 2023 (BIOVIA). Two parallel SWCNTs (6, 6) with the same length of 7.8 nm and an overlap length of 6.3 nm are aligned along *z*-direction. The tube-tube distance is set to be 2 nm. The two SWCNTs are sandwiched between

two parallel graphene sheets (GS), which cover the surface of SWCNTs with a minimum distance of 0.34 nm. The width of the graphene sheets is fixed at 4 nm with varying lengths of 2.6 nm, 3.9 nm, 5.2 nm, 6.5 nm, and 7.9 nm. Hydrogen atoms were added to the edges of the GS and CNT to mitigate the effects of unsaturation at the boundaries [64].To build the GS-w-CNT/PDMS nanocomposite model, PDMS chains with 10 monomers were packed into the system with a predefined density of 0.96 g/cm^3 using Amorphous Cell module. The masses of the GS, CNT and PDMS matrix can be calculated by counting the total numbers of atoms (mainly C, O Si and H) in GS, CNT and PDMS respectively. Therefore, the weight fraction can be calculated by dividing the total mass of GS and CNT by the overall mass of the GS-w-CNT/PDMS nanocomposite. Consequently, different GS-w-CNT/PDMS nanocomposite models with a fixed simulation cell of 4 nm×4 nm×10 nm were constructed.

Calculation of thermal conductivity: After establishing the GS-w-CNT/PDMS models, the structures are relaxed to an equilibrium state with minimum potential energy for further thermal conductivity calculation. COMPASS II, which is a force field that can precisely simulate the performance of polymer-based nanocomposites, is used to describe inter-atomic interactions [65]. 9-6 Lennard-Jones (LJ) potential was used to describe the van der Waals force between GS and CNT as follows:

$$V(r) = \varepsilon_0 \left[2\left(\frac{\sigma}{r}\right)^9 - 3\left(\frac{\sigma}{r}\right)^6 \right] \quad (6)$$

where σ denotes the zero–across distance of the potential, ε_0 represents the energy reflecting the interaction strength, and r is the distance of two atoms. Here, the $\sigma_{c\text{-}c}$ was set as 3.407 Å [65-67], and the cut-off distance is set as 10.5 Å [68], which is about three times of $\sigma_{c\text{-}c}$. Therefore, the initial gap between GS and CNT was set as 0.34 nm to guarantee the van der Waals interaction between them. A geometric optimization is firstly conducted using smart gradient algorithm. Then, the structures are relaxed in an NVT ensemble (constant number of atoms, volume and temperature) at 300 K for 200 ps followed by another relaxation *via* NPT ensemble (constant number of atoms, pressure and temperature) at 500 K and 1 atm for 200 ps to reach a reasonable density. Thereafter, the structures are cooled to 300 K at a rate of 1 K ps^{-1} in the NPT ensemble at 1atm to release uneven stress inside PDMS chains. Finally, the structures are optimized at 300 K for 200 ps by another NVT ensemble to guarantee strong interfacial bonding between GS-w-CNT and PDMS. Nose thermostat is used to maintain the temperature in all the NVT and NPT simulations [69].

The thermal conductivity of GS-w-CNT/PDMS is calculated by RNEMD method [70]. In the RNEMD, the whole simulation cell is divided into 120 slabs and two slabs at the ends are selected as the heat source and heat sink respectively. Simultaneously, the whole simulation is conducted in an NVE (constant number of atoms, volume and energy) ensemble. A heat flux is produced by the kinetic energy exchange between the atom with the highest kinetic energy in the heat source and that with the lowest kinetic energy in the heat sink. Once the system reaches a steady state, a constant heat flux (J) is established and a temperature gradient profile(∇T) is formed along the heat flux direction. The thermal conductivity then can be expressed according to Fourier law (Equation 7):

$$\kappa = -\frac{J}{\nabla T} \tag{7}$$

Calculation of vibrational power spectrum (VPS): The energy of atomic vibrations essentially reflects the thermal energy of the system. In the molecular dynamic simulation, VPS containing the entire distribution of the power of all atomic motions in frequency domain can be expressed by applying Fourier transform (FT) on atomic velocity autocorrelation functions (VAF) (Equation 8) [71]:

$$D(\omega) = \int_0^\tau \Gamma(t) cos\ (\omega t) dt \tag{8}$$

where D(ω)is VPS, ω is frequency, τ represents integration time, and Γ(t) stands for the VAF, which is determined by Equation 9 [55].

$$\Gamma(t) = \langle v(t)v(0) \rangle \tag{9}$$

where *v(t)* and *v(0)* are the atom velocity at time t and the beginning, <⋯> represents time related atom velocity autocorrelation function. In the simulation, τ is set as 5 ps and the velocity is correlated every 2 fs.

Supporting Information

Supporting Information is available from the Wiley Online Library or from the author.

Acknowledgements

F. Zhang and Y. Sun contributed to the work equally. This work was financially supported by University Development Fund (UDF0100152), the National Natural Science Foundation of China (52130303, 52327802, 52372096, 52102368, 22205189, 52203103), the Program for Guangdong Introducing Innovative and Entrepreneurial Teams (No. 2017ZT07C291),

Shenzhen Science and Technology Program (No. KQTD20170810141424366), Guang Dong Basic and Applied Basic Research Foundation (No. 2022A1515011010 and No. 2021A1515110350), Regional Joint Fund for Basic Research and Applied Basic Research of Guangdong Province (No. 2020SA001515110905), Shenzhen Natural Science Foundation (GXWD20201231105722002-20200824163747001). X.S. acknowledges the support from Research Grants Council of Hong Kong (GRF project: 16200720), start-up fund for new recruits (Nos. P0038855 and P0038858), and Research Institute for Sports Science and Technology of Hong Kong PolyU (No. P0043535).

Received: ((will be filled in by the editorial staff))
Revised: ((will be filled in by the editorial staff))
Published online: ((will be filled in by the editorial staff))

References

[1] F. Zhang, Y. Feng, W. Feng, *Mater. Sci. Eng. R Rep.* **2020**, 142, 100580.

[2] S. Xu, X.-L. Shi, M. Dargusch, C. Di, J. Zou, Z.-G. Chen, *Prog. Mater Sci.* **2021**, 121, 100840.

[3] C. Huang, X. Qian, R. Yang, *Mater. Sci. Eng. R Rep.* **2018**, 132, 1.

[4] X. Xu, J. Chen, J. Zhou, B. Li, *Adv. Mater.* **2018**, 30, 1705544.

[5] S. A. A. Jaleel, T. Kim, S. Baik, *Adv. Mater.* **2023**, 35, 2300956.

[6] L. Chen, T.-H. Liu, X. Wang, Y. Wang, X. Cui, Q. Yan, L. Lv, J. Ying, J. Gao, M. Han, J. Yu, C. Song, J. Gao, R. Sun, C. Xue, N. Jiang, T. Deng, K. Nishimura, R. Yang, C.-T. Lin, W. Dai, *Adv. Mater.* **2023**, 35, 2211100.

[7] Z. Xie, Z. Dou, D. Wu, X. Zeng, Y. Feng, Y. Tian, Q. Fu, K. Wu, *Adv. Funct. Mater.* **2023**, 33, 2214071.

[8] H. He, W. Peng, J. Liu, X. Y. Chan, S. Liu, L. Lu, H. Le Ferrand, *Adv. Mater.* **2022**, 34, 2205120.

[9] J. Han, G. Du, W. Gao, H. Bai, *Adv. Funct. Mater.* **2019**, 29, 1900412.

[10] Z. Wu, C. Xu, C. Ma, Z. Liu, H.-M. Cheng, W. Ren, *Adv. Mater.* **2019**, 31, 1900199.

[11] M. Cao, Z. Li, J. Lu, B. Wang, H. Lai, Z. Li, Y. Gao, X. Ming, S. Luo, L. Peng, Z. Xu, S. Liu, Y. Liu, C. Gao, *Adv. Mater.* **2023**, 35, 2300077.

[12] H. Yu, Y. Feng, C. Chen, Z. Zhang, Y. Cai, M. Qin, W. Feng, *Carbon* **2021**, 179, 348.

[13] L. Jing, R. Cheng, R. Garg, W. Gong, I. Lee, A. Schmit, T. Cohen-Karni, X. Zhang, S.

Shen, *ACS Nano* **2023**, 17, 2602.

[14] Q. Yan, F. E. Alam, J. Gao, W. Dai, X. Tan, L. Lv, J. Wang, H. Zhang, D. Chen, K. Nishimura, L. Wang, J. Yu, J. Lu, R. Sun, R. Xiang, S. Maruyama, H. Zhang, S. Wu, N. Jiang, C.-T. Lin, *Adv. Funct. Mater.* **2021**, 31, 2104062.

[15] H. Zhang, Q. He, H. Yu, M. Qin, Y. Feng, W. Feng, *Adv. Funct. Mater.* **2023**, 33, 2211985.

[16] Z. Luo, D. Yang, J. Liu, H.-Y. Zhao, T. Zhao, B.-X. Li, W.-G. Yang, Z.-Z. Yu, *Adv. Funct. Mater.* **2023**, 33, 2212032.

[17] X. Wu, H. Wang, Z. Wang, J. Xu, Y. Wu, R. Xue, H. Cui, C. Tian, Y. Wang, X. Huang, *Carbon* **2021**, 182, 445.

[18] F. Zhang, D. Ren, Y. Zhang, L. Huang, Y. Sun, W. Wang, Q. Zhang, W. Feng, Q. Zheng, *Chem. Eng. J.* **2022**, 431, 134102.

[19] B. Li, N. Wu, Y. Yang, F. Pan, C. Wang, G. Wang, L. Xiao, W. Liu, J. Liu, Z. Zeng, *Adv. Funct. Mater.* **2023**, 33, 2213357.

[20] K. M. F. Shahil, A. A. Balandin, *Nano Lett.* **2012**, 12, 861.

[21] A. A. Balandin, S. Ghosh, W. Bao, I. Calizo, D. Teweldebrhan, F. Miao, C. N. Lau, *Nano Lett.* **2008**, 8, 902.

[22] P. Kim, L. Shi, A. Majumdar, P. L. McEuen, *Phys. Rev. Lett.* **2001**, 87, 215502.

[23] C.-W. Chang-Jian, E.-C. Cho, K.-C. Lee, J.-H. Huang, P.-Y. Chen, B.-C. Ho, Y.-S. Hsiao, *Composites Part B* **2018**, 136, 46.

[24] Z. Han, A. Fina, *Prog. Mater Sci.* **2011**, 36, 914.

[25] S. Mohammad Nejad, R. Srivastava, F. M. Bellussi, H. Chávez Thielemann, P. Asinari, M. Fasano, *Int. J. Heat Mass Transfer* **2021**, 159, 106588.

[26] M. Biercuk, M. C. Llaguno, M. Radosavljevic, J. Hyun, A. T. Johnson, J. E. Fischer, *Appl. Phys. Lett.* **2002**, 80, 2767.

[27] J. C. Grunlan, Y. S. Kim, S. Ziaee, X. Wei, B. Abdel‐Magid, K. Tao, *Macromol Mater Eng* **2006**, 291, 1035.

[28] J. E. Peters, D. V. Papavassiliou, B. P. Grady, *Macromolecules* **2008**, 41, 7274.

[29] R. S. Prasher, X. Hu, Y. Chalopin, N. Mingo, K. Lofgreen, S. Volz, F. Cleri, P. Keblinski, *Phys. Rev. Lett.* **2009**, 102, 105901.

[30] S. N. Schiffres, K. H. Kim, L. Hu, A. J. McGaughey, M. F. Islam, J. A. Malen, *Adv. Funct. Mater.* **2012**, 22, 5251.

[31] J. Rafiee, X. Mi, H. Gullapalli, A. V. Thomas, F. Yavari, Y. Shi, P. M. Ajayan, N. A. Koratkar, *Nat. Mater.* **2012**, 11, 217.

[32] H. Zhong, J. R. Lukes, *Phys. Rev. B* **2006**, 74, 125403.

[33] V. Varshney, S. S. Patnaik, A. K. Roy, G. Froudakis, B. L. Farmer, *ACS Nano* **2010**, 4, 1153.

[34] V. Varshney, A. K. Roy, G. Froudakis, B. L. Farmer, *Nanoscale* **2011**, 3, 3679.

[35] J. Chen, J. H. Walther, P. Koumoutsakos, *Adv. Funct. Mater.* **2015**, 25, 7539.

[36] M. Su, G. Han, J. Gao, Y. Feng, C. He, J. Ma, C. Liu, C. Shen, *Chem. Eng. J.* **2022**, 427, 131665.

[37] X. Yang, D. Chen, Z. Han, X. Ma, A. C. To, *Int. J. Heat Mass Transfer* **2014**, 70, 803.

[38] F. Zhang, D. Ren, L. Huang, Y. Zhang, Y. Sun, D. Liu, Q. Zhang, W. Feng, Q. Zheng, *Adv. Funct. Mater.* **2021**, 31, 2107082.

[39] F. Zhang, Y. Feng, M. Qin, T. Ji, F. Lv, Z. Li, L. Gao, P. Long, F. Zhao, W. Feng, *Carbon* **2019**, 145, 378.

[40] F. Xue, X.-z. Jin, X. Xie, X.-d. Qi, J.-h. Yang, Y. Wang, *Nanoscale* **2019**, 11, 18691.

[41] W. Dai, J. Yu, Y. Wang, Y. Song, F. E. Alam, K. Nishimura, C.-T. Lin, N. Jiang, *J. Mater. Chem. A* **2015**, 3, 4884.

[42] F. Zhang, Y. Feng, M. Qin, L. Gao, Z. Li, F. Zhao, Z. Zhang, F. Lv, W. Feng, *Adv. Funct. Mater.* **2019**, 29, 1901383.

[43] S.-S. Yoon, D.-Y. Khang, *Nano Lett.* **2016**, 16, 3550.

[44] E. C. Garnett, W. Cai, J. J. Cha, F. Mahmood, S. T. Connor, M. Greyson Christoforo, Y. Cui, M. D. McGehee, M. L. Brongersma, *Nat. Mater.* **2012**, 11, 241.

[45] M. B. Vazquez-Santos, E. Geissler, K. Laszlo, J.-N. Rouzaud, A. Martinez-Alonso, J. M. Tascón, *J. Phys. Chem. C* **2012**, 116, 257.

[46] W. Zhao, Y. Li, S. Wang, X. He, Y. Shang, Q. Peng, C. Wang, S. Du, X. Gui, Y. Yang, *Carbon* **2014**, 76, 19.

[47] S. Tsuzuki, A. Fujii, *Phys. Chem. Chem. Phys.* **2008**, 10, 2584.

[48] A. Beigbeder, M. Linares, M. Devalckenaere, P. Degée, M. Claes, D. Beljonne, R. Lazzaroni, P. Dubois, *Adv. Mater.* **2008**, 20, 1003.

[49] S. M. M. Zamani, K. Behdinan, *Compos Sci Technol.* **2020**, 200, 108463.

[50] T. Luo, K. Esfarjani, J. Shiomi, A. Henry, G. Chen, *J. Appl. Phys.* **2011**, 109. 074321.

[51] R. H. Gee, R. S. Maxwell, B. Balazs, *Polymer* **2004**, 45, 3885.

[52] Y. Du, S. Liu, S. Yuan, H. Zhang, S. Yuan, *Colloid Surface A* **2021**, 618, 126409.

[53] S. Maruyama, *Physica B Condens. Matter* **2002**, 323, 193.

[54] H. Y. Chiu, V. V. Deshpande, H. W. C. Postma, C. N. Lau, C. Mikó, L. Forró, M. Bockrath, *Phys. Rev. Lett.* **2005**, 95, 226101.

[55] X. Shen, Z. Wang, Y. Wu, X. Liu, J.-K. Kim, *Carbon* **2016**, 108, 412.

[56] D. Donadio, G. Galli, *Phys. Rev. Lett.* **2007**, 99, 255502.

[57] F. Giannazzo, S. Sonde, R. L. Nigro, E. Rimini, V. Raineri, *Nano Lett.* **2011**, 11, 4612.

[58] X. Shen, Z. Wang, Y. Wu, X. Liu, Y.-B. He, J.-K. Kim, *Nano Lett.* **2016**, 16, 3585.

[59] P. J. O'Brien, S. Shenogin, J. Liu, P. K. Chow, D. Laurencin, P. H. Mutin, M. Yamaguchi, P. Keblinski, G. Ramanath, *Nat. Mater.* **2013**, 12, 118.

[60] M. D. Losego, M. E. Grady, N. R. Sottos, D. G. Cahill, P. V. Braun, *Nat Mater.* **2012**, 11, 502.

[61] X. Ma, S. Wu, Z. Yi, D. Peng, J. Zhang, *Int. J. Heat Mass Transfer* **2019**, 137, 790.

[62] Z. Wang, J. Li, K. Yuan, *Int. J. Therm. Sci.* **2018**, 132, 589.

[63] D. Liu, C. Lei, K. Wu, Q. Fu, *ACS Nano* **2020**, 14, 15738.

[64] Q. Zheng, Y. Geng, S. Wang, Z. Li, J.-K. Kim, *Carbon* **2010**, 48, 4315.

[65] H. Sun, Z. Jin, C. Yang, R. L. Akkermans, S. H. Robertson, N. A. Spenley, S. Miller, S. M. Todd, *J Mol Model* **2016**, 22, 47.

[66] R. Saito, R. Matsuo, T. Kimura, G. Dresselhaus, M. S. Dresselhaus, *Chem. Phys. Lett.* **2001**, 348, 187.

[67] J. Dong, L. Cao, Y. Li, Z. Wu, C. Teng, *Compos Sci Technol.* **2020**, 196, 108242.

[68] B. Liu, J. A. Baimova, C. D. Reddy, A. W.-K. Law, S. V. Dmitriev, H. Wu, K. Zhou, *ACS Appl. Mater. Interfaces* **2014**, 6, 18180.

[69] J.-L. Tsai, S.-H. Tzeng, Y.-T. J. C. P. B. E. Chiu, *Composites Part B* **2010**, 41, 106.

[70] F. Müller-Plathe, *J. Chem. Phys.* **1997**, 106, 6082.

[71] T. Luo, J. R. Lloyd, *Adv. Funct. Mater.* **2012**, 22, 2495.

Graphitic structure welded carbon nanotube network is produced by interfacial welding. The introduced graphic structure significantly reduce the thermal resistance in carbon nanotube junction and endows the composite with a high thermal conductivity of 5.58 W m^{-1} K^{-1}, which is 4.1 times higher than that of pristine carbon nanotube network.

Fei Zhang, Yuxuan Sun, Lei Guo, Yinhang Zhang, Dan Liu, Wei Feng*, Xi Shen* , Qingbin Zheng*

Microstructural Welding Engineering of Carbon Nanotube/Polydimethylsiloxane Nanocomposites with Improved Interfacial Thermal Transport

ToC figure